

Interplay of wavelength, fluence and spot-size in free-electron laser ablation of cornea

M. Shane Hutson^{1-3*}, Borislav Ivanov¹, Aroshan Jayasinghe¹, Gilma Adunas¹, Yaowu Xiao¹, Mingsheng Guo⁴, John Kozub²

¹Department of Physics & Astronomy, Vanderbilt University, Nashville, TN 37235, USA

²W.M. Keck Vanderbilt Free-electron Laser Center, Vanderbilt University, Nashville, TN 37235, USA

³Vanderbilt Institute for Integrative Biosystem Research & Education, Vanderbilt University, Nashville, TN 37235, USA

⁴Department of Physics, Fisk University, Nashville, TN 37208, USA

*shane.hutson@vanderbilt.edu

Abstract: Infrared free-electron lasers ablate tissue with high efficiency and low collateral damage when tuned to the 6-μm range. This wavelength-dependence has been hypothesized to arise from a multi-step process following differential absorption by tissue water and proteins. Here, we test this hypothesis at wavelengths for which cornea has matching overall absorption, but drastically different differential absorption. We measure etch depth, collateral damage and plume images and find that the hypothesis is not confirmed. We do find larger etch depths for larger spot sizes – an effect that can lead to an apparent wavelength dependence. Plume imaging at several wavelengths and spot sizes suggests that this effect is due to increased post-pulse ablation at larger spots.

©2009 Optical Society of America

OCIS codes: (140.2600) Free-electron lasers (FELs); (170.1020) Ablation of tissue

References and links

1. G. Edwards, R. Logan, M. Copeland, L. Reinisch, J. Davidson, B. Johnson, R. Maciunas, M. Mendenhall, R. Ossoff, J. Tribble, J. Werkhaven, and D. O'Day, "Tissue ablation by a free-electron laser tuned to the amide II band," *Nature* **371**(6496), 416–419 (1994).
2. J. I. Youn, P. Sweet, G. M. Peavy, and V. Venugopalan, "Mid-IR laser ablation of articular and fibro-cartilage: a wavelength dependence study of thermal injury and crater morphology," *Lasers Surg. Med.* **38**(3), 218–228 (2006).
3. K. M. Joos, J. H. Shen, D. J. Shetlar, and V. A. Casagrande, "Optic nerve sheath fenestration with a novel wavelength produced by the free electron laser (FEL)," *Lasers Surg. Med.* **27**(3), 191–205 (2000).
4. R. A. Hill, Q. Ren, D. C. Nguyen, L. H. Liaw, and M. W. Berns, "Free-electron laser (FEL) ablation of ocular tissues," *Lasers Med. Sci.* **13**(3), 219–226 (1998).
5. R. Kaufmann, and R. Hibst, "Pulsed erbium:YAG laser ablation in cutaneous surgery," *Lasers Surg. Med.* **19**(3), 324–330 (1996).
6. R. Cubeddu, C. Sozzi, P. Taroni, G. Valentini, G. Bottiroli, and A. C. Croce, "Study of mechanical and thermal damage in brain tissue after ablation by Erbium-YAG laser," *Lasers Med. Sci.* **12**(1), 21–30 (1997).
7. T. S. Alster, "Clinical and histologic evaluation of six erbium:YAG lasers for cutaneous resurfacing," *Lasers Surg. Med.* **24**(2), 87–92 (1999).
8. J. Kiefer, J. Tillein, Q. Ye, R. Klinke, and W. Gstoettner, "Application of carbon dioxide and erbium:yttrium-aluminum-garnet lasers in inner ear surgery: an experimental study," *Otol. Neurotol.* **25**(3), 400–409 (2004).
9. G. S. Edwards, R. H. Austin, F. E. Carroll, M. L. Copeland, M. E. Couplie, W. E. Gabella, R. F. Haglund, B. A. Hooper, M. S. Hutson, E. D. Jansen, K. M. Joos, D. P. Kiehart, I. Lindau, J. Miao, H. S. Pratisto, J. H. Shen, Y. Tokutake, A. F. G. van der Meer, and A. Xie, "Free-electron-laser-based biophysical and biomedical instrumentation," *Rev. Sci. Instrum.* **74**(7), 3207–3245 (2003).
10. M. L. Copeland, R. J. Maciunas, and G. S. Edwards, "Chapter VII," in *Neurosurgical Topics: Advanced Techniques in Central Nervous System Metastases*, R. J. Maciunas, ed. (The American Association of Neurological Surgeons, Park Ridge, IL, 1998).
11. G. S. Edwards, R. D. Pearlstein, M. L. Copeland, M. S. Hutson, K. Latone, A. Spiro, and G. Pasmanik, "6450 nm wavelength tissue ablation using a nanosecond laser based on difference frequency mixing and stimulated Raman scattering," *Opt. Lett.* **32**(11), 1426–1428 (2007).
12. M. A. Mackanos, D. Simanovskii, K. M. Joos, H. A. Schwettman, and E. D. Jansen, "Mid infrared optical parametric oscillator (OPO) as a viable alternative to tissue ablation with the free electron laser (FEL)," *Lasers Surg. Med.* **39**(3), 230–236 (2007).

13. M. S. Hutson, S. A. Hauger, and G. Edwards, "Thermal diffusion and chemical kinetics in laminar biomaterial due to heating by a free-electron laser," *Phys. Rev. E Stat. Nonlin. Soft Matter Phys.* **65**(6 Pt 1), 061906 (2002).
14. G. S. Edwards, and M. S. Hutson, "Advantage of the Mark-III FEL for biophysical research and biomedical applications," *J. Synchrotron Radiat.* **10**(5), 354–357 (2003).
15. M. S. Hutson, and G. S. Edwards, "Advances in the Physical Understanding of Laser Surgery at 6.45 microns," in *26th International Free Electron Laser Conference and 11th FEL Users Workshop* (Trieste, Italy, 2003) paper: FRAIS01.
16. V. Venugopalan, N. S. Nishioka, and B. B. Mikić, "Thermodynamic response of soft biological tissues to pulsed infrared-laser irradiation," *Biophys. J.* **70**(6), 2981–2993 (1996).
17. J. Tribble, D. C. Lamb, L. Reinisch, and G. Edwards, "Dynamics of gelatin ablation due to free-electron-laser irradiation," *Phys. Rev. E Stat. Phys. Plasmas Fluids Relat. Interdiscip. Topics* **55**(6), 7385–7389 (1997).
18. W. Wagner, A. Sokolow, R. D. Pearlstein, and G. S. Edwards, "Thermal vapor bubble and pressure dynamics during infrared laser ablation of tissue," *Appl. Phys. Lett.* **94**(1), 013901 (2009).
19. Y. W. Xiao, M. S. Guo, K. Parker, and M. S. Hutson, "Wavelength-dependent collagen fragmentation during mid-IR laser ablation," *Biophys. J.* **91**(4), 1424–1432 (2006).
20. Y. Xiao, M. Guo, P. Zhang, G. Shanmugam, P. L. Polavarapu, and M. S. Hutson, "Wavelength-dependent conformational changes in collagen after mid-infrared laser ablation of cornea," *Biophys. J.* **94**(4), 1359–1366 (2008).
21. M. A. Mackanos, J. A. Kozub, and E. D. Jansen, "The effect of free-electron laser pulse structure on mid-infrared soft-tissue ablation: ablation metrics," *Phys. Med. Biol.* **50**(8), 1871–1883 (2005).
22. M. A. Mackanos, J. A. Kozub, D. L. Hachey, K. M. Joos, D. L. Ellis, and E. D. Jansen, "The effect of free-electron laser pulse structure on mid-infrared soft-tissue ablation: biological effects," *Phys. Med. Biol.* **50**(8), 1885–1899 (2005).
23. J. M. J. Madey, "Stimulated Emission of Bremsstrahlung in a Periodic Magnetic Field," *J. Appl. Phys.* **42**(5), 1906–1930 (1971).
24. A. Vogel, and V. Venugopalan, "Mechanisms of pulsed laser ablation of biological tissues," *Chem. Rev.* **103**(2), 577–644 (2003).
25. W. B. Telfair, C. Bekker, H. J. Hoffman, P. R. Yoder, Jr., R. E. Nordquist, R. A. Eiferman, and H. H. Zenzie, "Histological comparison of corneal ablation with Er:YAG laser, Nd:YAG optical parametric oscillator, and excimer laser," *J. Refract. Surg.* **16**(1), 40–50 (2000).
26. B. P. Payne, N. S. Nishioka, B. B. Mikic, and V. Venugopalan, "Comparison of pulsed CO₂ laser ablation at 10.6 μm and 9.5 μm," *Lasers Surg. Med.* **23**(1), 1–6 (1998).
27. Y. Domankevitz, M. S. Lee, and N. S. Nishioka, "Effects of irradiance and spot size on pulsed holmium laser ablation of tissue," *Appl. Opt.* **32**(4), 569–573 (1993).
28. U. S. Sathyam, A. Shearin, and S. A. Prahl, "The effects of spot size, pulse energy, and repetition rate on microsecond ablation of gelatin under water," *Proc. SPIE-Int. Soc. Opt. Eng.* **2391**, 336–344 (1995).
29. U. S. Sathyam, A. Shearin, E. A. Chasteney, and S. A. Prahl, "Threshold and ablation efficiency studies of microsecond ablation of gelatin under water," *Lasers Surg. Med.* **19**(4), 397–406 (1996).
30. R. R. Anderson, and J. A. Parrish, "The optics of human skin," *J. Invest. Dermatol.* **77**(1), 13–19 (1981).
31. B. Wolff-Rottke, J. Ihlemann, H. Schmidt, and A. Scholl, "Influence of the laser spot diameter on photo-ablation rates," *Appl. Phys., A Mater. Sci. Process.* **60**(1), 13–17 (1995).
32. M. Eyett, and D. Bauerle, "Influence of the Beam Spot Size on Ablation Rates in Pulsed-Laser Processing," *Appl. Phys. Lett.* **51**(24), 2054–2055 (1987).
33. F. Partovi, J. A. Izatt, R. M. Cothren, C. Kittrell, J. E. Thomas, S. Strikwerda, J. R. Kramer, and M. S. Feld, "A model for thermal ablation of biological tissue using laser radiation," *Lasers Surg. Med.* **7**(2), 141–154 (1987).
34. B. Majaron, P. Plestenjak, and M. Lukac, "Thermo-mechanical laser ablation of soft biological tissue: modeling the micro-explosions," *Appl. Phys. B* **69**, 71–80 (1999).
35. A. Vogel, I. Apitz, and V. Venugopalan, "Phase transitions, material ejection, and plume dynamics in pulsed laser ablation of soft biological tissues," in *Oscillations, Waves and Interactions*, T. Kurz, U. Parlitz, and U. Kaatze, eds. (Universitätsverlag Göttingen, Göttingen, 2007), pp. 217–258.
36. I. Apitz, and A. Vogel, "Material ejection in nanosecond Er:YAG laser ablation of water, liver and skin," *Appl. Phys., A Mater. Sci. Process.* **81**(2), 329–338 (2005).
37. A. D. Zweig, "A thermo-mechanical model for laser ablation," *J. Appl. Phys.* **70**(3), 1684–1691 (1991).
38. J. P. Cummings, and J. T. Walsh, Jr., "Tissue tearing caused by pulsed laser-induced ablation pressure," *Appl. Opt.* **32**(4), 494 (1993).
39. J. I. Youn, P. Sweet, and G. M. Peavy, "A comparison of mass removal, thermal injury, and crater morphology of cortical bone ablation using wavelengths 2.79, 2.9, 6.1, and 6.45 microm," *Lasers Surg. Med.* **39**(4), 332–340 (2007).
40. J. M. Auerhammer, R. Walker, A. F. G. van der Meer, and B. Jean, "Dynamic behavior of photoablation products of corneal tissue in the mid-IR: a study with FELIX," *Appl. Phys. B* **68**(1), 111–119 (1999).

1. Introduction

Infrared free-electron lasers (FELs) can ablate soft biological tissues with high efficiency and remarkably little collateral damage. This is particularly true when an FEL is tuned to the 6-μm wavelength range [1]. For some tissues, the optimal wavelength is 6.1 μm [2] – corresponding to the overlapping peaks of the amide I vibrational mode of proteins and the bending mode of

water. For others, it is 6.45 μm [1,3] – corresponding to the tail of the water bending mode and the peak of the amide II vibrational mode of proteins. For others, it is closer to 6.0 μm [4]. In all tissues examined, both peaks were superior to wavelengths near 3.0 μm – corresponding to the peak of the water OH stretching mode. This last observation is not without controversy. Other lasers operating near 3.0 μm can also ablate soft tissues efficiently and with little collateral damage [5–8]. Nonetheless, the Vanderbilt FEL has been used to carry out eight successful human surgeries [9,10]; and tabletop lasers in the 6- μm range are under development to translate this success to more widespread surgical use [11,12].

Our current understanding of this wavelength-dependence is based on the fact that the 6- μm range directly targets protein vibrations [13–15]. Researchers have long hypothesized that such direct excitation could lead to a loss of protein structural integrity [1]. This structural failure should then allow tissue removal to occur at lower energy densities and a smaller pressure head, i.e. more efficiently and with less collateral damage. The hypothetical loss of structural integrity has two main difficulties. First, photon energies in the 6- μm range are quite low (~ 0.2 eV), so a photochemical mechanism is unlikely. Second, heat diffusion between a tissue's structural collagen fibers and the surrounding water is expected to take place on quite short time scales – just a few ns for the 30-nm diameter fibers in cornea. Thus, an FEL macropulse is much too long (3–5 μs) to confine the deposited energy to its original water or protein compartment, i.e. too long to achieve microscale thermal confinement [16].

On the other hand, the macropulse-width is not the only relevant time scale. Previous studies of FEL ablation considered fluences up to $200 \times$ the ablation threshold [1], where tissue removal begins well before the end of a macropulse [17,18]. In such cases, partial microscale thermal confinement could be achieved during times prior to the onset of vaporization. This idea has been modeled quantitatively by considering differential absorption by tissue water and collagen fibrils, heat diffusion between the two, and the temperature-dependent chemical kinetics of water vaporization and collagen denaturation [13–15]. This differential-absorption/partial-confinement model suggested a plausible mechanism for the original hypothesis: at high fluence, tissue water can begin explosive vaporization on the 10–100 ns time scale; during this time, partial thermal confinement leads to wavelength-dependent, protein-vs.-water temperature differentials; these in turn lead to wavelength-dependent collagen denaturation – amplified by the exponential dependence of chemical kinetics on $-1/T$ [13]. By the time explosive vaporization begins, the wavelength-dependent accumulation of denatured collagen determines whether the tissue structural matrix is strong and ductile or weak and brittle. In support of this model, recent experiments have confirmed wavelength-dependent denaturation and fragmentation of tissue collagen [19,20]. This model also successfully predicted that the FEL ablation metrics should be only weakly dependent on the FEL micropulse intensity [13,21,22]. The most important remaining prediction is the interplay between the wavelength-dependence and macropulse intensity [15]. At low intensities, the differential heating of water and protein is washed out by heat diffusion – microscale thermal confinement is not achieved prior to vaporization – leading to predicted ablation metrics that are independent of the targeted chromophore. As the intensity increases, partial microscale thermal confinement is achieved and differential heating drives larger and larger protein-water temperature differences – leading to the prediction of an increasingly strong wavelength-dependence. For the geometry of cornea and for wavelengths with similar absorption as at 6.45 μm , the targeted chromophore is predicted to become important above 3×10^6 W/cm² [14,15]. In this report, we test this prediction of a coupled wavelength and intensity dependence and find that it is not confirmed by experiments. Interestingly, we do find a spot-size dependence in the metrics that can masquerade as wavelength dependence.

2. Materials & methods

Corneas were obtained from sacrificed pig eyes within 24 hours post-mortem, swabbed with ethanol to remove the epithelial layer, and washed with distilled water to remove any contaminant on the surface. For each tissue sample, a strip of cornea and sclera (approximately 5 × 1 cm) was affixed over the internal opening of a metal substrate (razor

blade) using cyanoacrylate glue applied to the edges of the strip. Special care was taken to ensure uniform tension on the sample and avoid any wrinkling of the surface. Corneal samples were periodically sprayed with saline, with the excess carefully blotted away, to maintain normal hydration. The thickness of the cornea was measured with a micrometer caliper.

2.1 Laser parameters

The Vanderbilt Mark-III FEL has a complex pulse structure in which 3-5 μ s long macropulses are delivered at 1-30 Hz [23]. Each macropulse is composed of a micropulse train: 1-ps long pulses at a repetition rate of 2.85 GHz. Note that all references to fluence in this report correspond to macropulse fluence. For each experiment, the FEL is tuned to a specific wavelength in the range 2-9 μ m (with linewidth $\Delta\lambda/\lambda \sim 2\%$ FWHM). Measurements were conducted at a pulse repetition rate of 30 Hz (except single-pulse plume imaging).

At the experimental end station, the FEL exits an evacuated beam transport system with a $1/e^2$ radius from 5 to 10 mm (wavelength-dependent) and a Rayleigh range in excess of 10 m. The beam is steered by three 3"-diameter silver-coated mirrors and traverses a large-aperture shutter (Uniblitz VS35S27M1, Vincent Associates, Rochester, NY), a wire-grid polarizer for fine energy control, an adjustable iris aperture, a CaF₂ pickoff window that sends a small fraction of the beam (~10%) to an energy meter (Ophir PE50BB, Ophir-Spiricon, Logan, UT), and a planoconvex lens to focus the beam (CaF₂, nominal $f = 10, 15, 25$ or 50 cm at $\lambda = 5 \mu$ m; all optics from ISP Optics, Irvington, NY). A second energy meter was placed behind the sample. In some experiments, the wire grid was replaced with a Brewster angle polarizer.

2.2 Beam profile measurements

The intensity profile of the FEL beam was measured at multiple locations near the focus using a knife-edge technique. Measurements were made in two orthogonal directions at several points along the beam to calculate the focal plane, minimum beam waist and Rayleigh length. The FEL pulse energy was kept at 0.5 mJ during the profile measurement to avoid damage to the razor blade's edge.

2.3 Etch depth measurements

Cornea samples were positioned such that the sample surface was at the FEL focal plane. These samples were generally thinner than the Rayleigh range of the focused beam (except for $f = 10$ cm). Each measurement consisted of measuring the number of pulses required to perforate the sample – detected by an energy meter placed behind the sample. The pre-perforation pulses were counted and measured by sending a small fraction of every pulse to a calibrated energy meter. Each perforation was conducted at a fresh spot on the sample, with a spot separation of 1 mm in both directions. Five to eight such perforations were measured for each set of laser parameters (wavelength, pulse energy and focused beam radius). The mean etch depth per pulse is the corneal thickness divided by the average number of pulses required for perforation. The results were subjected to nonlinear regression in Origin (OriginLab Corporation, Northampton, MA) and statistical analysis in Mathematica (Wolfram Research, Champaign, IL).

2.4 Histology for collateral damage analysis

Samples were mounted as above and most were exposed to FEL macropulses at a rate of 30 Hz while the sample was translated at 0.3 mm/s – resulting in a long, linear crater. For other samples, a linear crater was created by exposure to a fixed number of pulses at one location, translation by approximately half a beam diameter, and repeated exposure, with the cycle repeated dozens of times. Six to eight lines were cut into each cornea, with different macropulse fluence for each line. Ablated samples were fixed, imbedded in paraffin and sectioned at 6- μ m intervals perpendicular to the tissue surface and the linear incision. Sections were mounted on 1 × 3 inch glass slides and stained with hematoxylin and eosin.

The crater morphology and zone of thermal injury were examined by bright-field microscopy. The darker areas along the edges of the crater are regions of thermal collateral

damage [22]. The extent of these regions was quantified using ImageJ (NIH, Bethesda, MD). We first thresholded the contiguous dark region along the crater borders and then analyzed its thickness from 10% to 90% of the crater depth. The resulting distributions of collateral damage thickness were characterized in terms of their mean, median and quartile boundaries.

2.5 Plume imaging

Samples were mounted as described above, and the pulse energy was adjusted to maintain a constant fluence of 15 J/cm^2 . The ablation plume was imaged perpendicular to the FEL beam path using a nitrogen laser (LN1000, Laser Photonics LLC, Lake Mary, FL) coupled to a rhodamine dye module (Laser Photonics LN102) to produce a 4 ns pulse of light at $\lambda = 644 \text{ nm}$. To reduce laser speckle and improve image quality, the laser was coupled into a 1-km long multimode optical fiber. A 25-mm planoconvex lens collimated the output from the fiber to produce a beam that passed in front of, and parallel to, the sample stage. The resulting image was focused onto the sensor of a color CCD camera (AVT Dolphin F145C, Allied Vision Technologies, Stadtroda, Germany) using a 105-mm zoom lens (Nikon Telephoto AF, Nikon Co., Tokyo, Japan). A digital delay/pulse generator (SRS DG535, Stanford Research Systems, Sunnyvale, CA) and custom-built synchronization circuit were used to set the delay between the ablation and illumination lasers [22].

3. Results

To test the differential-absorption/partial-confinement model, we ablated porcine corneas with the FEL at a variety of wavelengths, spot-sizes and fluence. The chosen wavelengths were 2.77, 3.32, 5.97, 6.26 and $6.45 \mu\text{m}$ – five wavelengths for which cornea has matching absorption coefficients, but which differentially target protein and water (Table 1). Among these wavelengths, the model predicts no chromophore-dependence for the ablation metrics at low macropulse intensity – $< 3 \times 10^6 \text{ W/cm}^2$, equivalent to a fluence of 15 J/cm^2 [15] – and an increasingly strong dependence at high fluence. In the high-fluence regime, wavelengths that target protein are predicted to have higher ablation efficiency and lower collateral damage. The experiments below cover a wide range of fluence, 5 to 250 J/cm^2 , and examine the ablation process in terms of etch depth, collateral damage and plume images.

Table 1. Effective absorption coefficient, α , for FEL irradiation of corneal stroma^a – including estimates for its water and protein components.^b

Wavelength (μm)	$1/\alpha_{\text{cornea}} (\mu\text{m})$	$1/\alpha_{\text{protein}} (\mu\text{m})$	$1/\alpha_{\text{water}} (\mu\text{m})$	$\alpha_{\text{protein}}/\alpha_{\text{water}}$
2.77	5.4	20.1	4.8	0.24
3.32	5.4	7.0	5.2	0.74
5.97	5.2	3.4	5.7	1.7
6.26	5.1	3.0	5.8	2.0
6.45	5.9	1.7	10.1	5.8

^aBased on a Gaussian-weighted average over the FEL linewidth (FWHM = $2\% \lambda$) using spectra from [15].

^bAssumes a composite corneal spectrum representing 85% water and 15% protein by volume.

3.1 Etch depth

As a first test, we measured the mean etch depth per pulse δ as a function of wavelength λ and single-pulse fluence Φ . Even within the matched set of wavelengths, the slope of $\delta(\Phi)$ is highly chromophore-dependent. As shown in Fig. 1(a), the slope is much larger for the wavelengths that predominantly target protein modes (5.97, 6.26 and $6.45 \mu\text{m}$). This larger slope indicates higher ablation efficiency.

At first glance, the data appear to strongly confirm the model predictions; however, these data were collected using a single focusing lens. The wavelength is thus tightly coupled with the focal spot size ($w = 1/e^2$ radius at the beam waist). To decouple λ and w , we collected additional data with different focal-length lenses. In some instances, we further varied w by placing a variable aperture before the lens. In this second data set, the slope of $\delta(\Phi)$ is highly spot-size-dependent – even for a single wavelength. Results for $\lambda = 2.77 \mu\text{m}$ are shown in Fig.

1(b). At the largest beam radius, this water-targeting wavelength has higher ablation efficiency than any of the protein-targeting wavelengths, but at the smallest beam radius, its efficiency is 1/10th as high. For protein-targeting wavelengths, the efficiency also decreases at smaller spot sizes, but in a much less drastic manner. One can see this effect in Fig. 1(a). Within the scatter of protein-targeting data, those points corresponding to the largest, middle and smallest spot sizes are on the corresponding high side, middle and low side of the range (open squares, circles and triangles respectively).

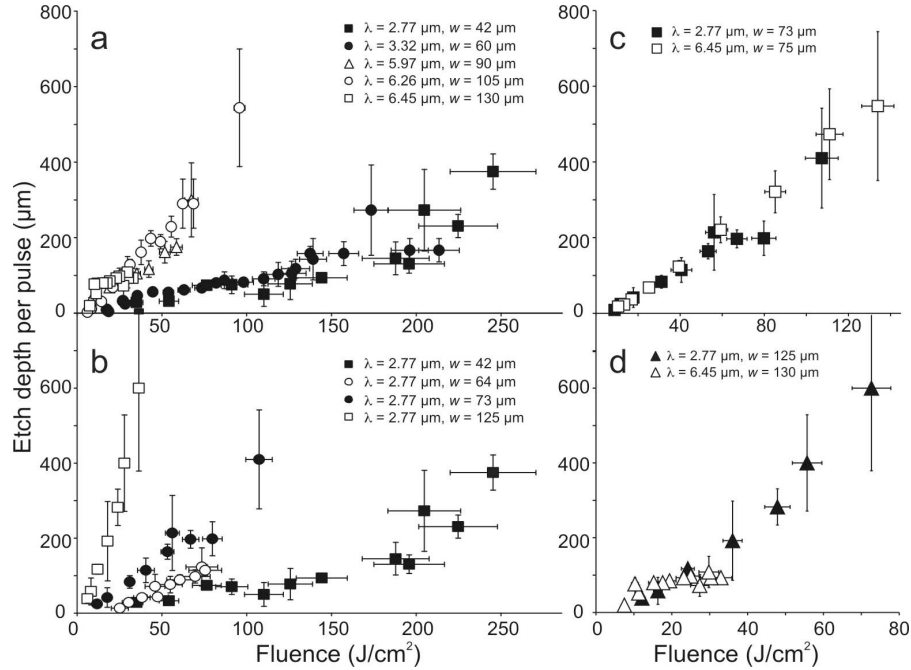


Fig. 1. Wavelength, fluence and spot-size dependence of the mean etch depth per pulse. (a) Several wavelengths with matched absorption coefficients. Each wavelength was focused with the same lens and thus has a different $1/e^2$ radius at the beam waist (w , noted in the legend). Open (closed) symbols are used for predominantly protein- (water)-targeting wavelengths. (b) A single wavelength focused with several different lenses to yield different spot-sizes. (c, d) Two wavelengths with distinct differential absorption, but closely matched spot sizes. Error bars correspond to \pm one standard deviation.

These observations raise an important question: how much of the apparent λ -dependence in Fig. 1(a) can be attributed to a coupled spot-size dependence? As a first test, we directly compare etch-depth measurements at different λ , but closely matched spot sizes. Even for the two wavelengths that appear most different in Fig. 1(a), 2.77 and 6.45 μm , measurements of $\delta(\Phi)$ overlap strongly when both wavelengths are focused to $w \sim 75 \mu\text{m}$ (Fig. 1(c)). An overlap also occurs at larger matched spot sizes ($w \sim 125 \mu\text{m}$), but we only have comparable data for $\Phi < 40 \text{ J/cm}^2$. At the high end of this range, the measurements hint at some wavelength differences. We do not have direct comparisons for $w < 70 \mu\text{m}$.

As a second test, we used linear regression to estimate the slope, or ablation efficiency, of $\delta(\Phi)$ for each w and λ in Fig. 1 plus several additional data sets (23 total). The efficiencies were then subjected to an analysis of covariance (ANCOVA) to determine whether there is a significant λ -dependence above and beyond the obvious spot-size dependence. ANCOVA was carried out using one factor – whether the wavelength dominantly targets protein or water – and one covariate, either $F(w) = w$ or w^2 . This makes the fitted model $a + bF(w) + c*target$, where $target = 0$ for protein-targeting wavelengths and $target = 1$ for water-targeting wavelengths. As expected, we find a highly significant dependence of ablation efficiency on either w or w^2 ($P = 5 \times 10^{-4}$ or 2×10^{-4}). The data do not provide tight enough constraints to

decide between these two forms of w -dependence; however, once the variance attributable to either $F(w)$ is removed, there is no remaining dependence on the targeted chromophore ($P_{\text{target}} = 0.35$ when $F(w) = w$; 0.38 when $F(w) = w^2$).

Despite capturing the trends in ablation efficiency, linear regression provides poor fits for those $\delta(\Phi)$ data sets that have obviously negative second derivatives (e.g. $\lambda = 6.45 \mu\text{m}$ and $w = 130 \mu\text{m}$ in Fig. 1(d)). To better parameterize all the etch depth data, we used nonlinear regression with a phenomenological Hibst model [24]:

$$\delta(\Phi) = \frac{\Phi_{\text{th}}}{\gamma \rho h_{\text{abl}}} \ln \left[1 + \gamma \left(\frac{\Phi - \Phi_{\text{th}}}{\Phi_{\text{th}}} \right) \right] \quad (1)$$

where ρ is the tissue density (1.062 g/cm^3), Φ_{th} is the threshold fluence, h_{abl} is the heat of ablation and γ varies between 0 and 1. In the original Hibst formulation, $\rho h_{\text{abl}}/\Phi_{\text{th}} = \mu_a$ was the tissue absorption coefficient and γ was a measure of plume shielding; however, one should not over-interpret the fitting results [24]; γ is best considered an indicator of whether $\delta(\Phi)$ behaves more like a blow-off model ($\gamma = 1$) or a steady-state model (limit $\gamma \rightarrow 0$). In either case, $1/(\rho h_{\text{abl}})$ is a measure of ablation efficiency and corresponds to the slope of $\delta(\Phi)$ just above threshold. The fitted parameters are plotted versus spot-size in Fig. 2. As the spot becomes more tightly focused, h_{abl} increases – quite rapidly for $2w < 150 \mu\text{m}$. Note that an increase in h_{abl} corresponds to a decrease in the slope of $\delta(\Phi)$, so this is another way to capture the spot-size dependence evident in Fig. 1. Tighter focus also increases Φ_{th} (Fig. 2(b)), but there is no obvious trend for γ .

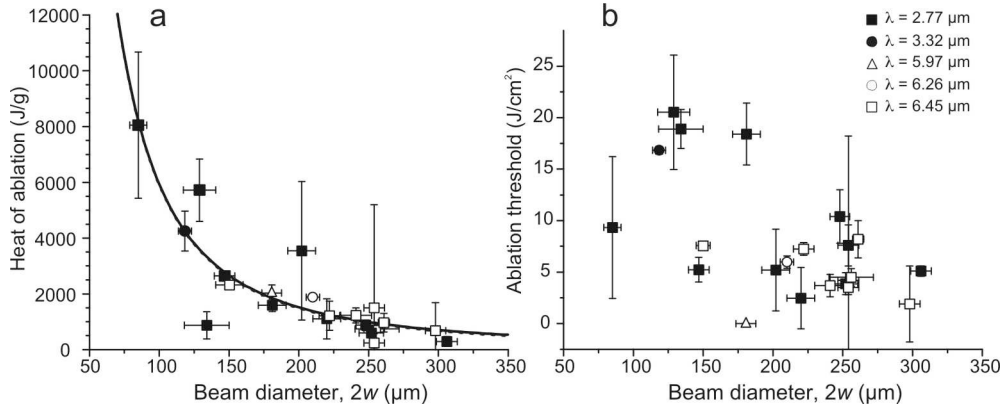


Fig. 2. Wavelength and spot-size dependence for the Hibst model parameters: (a) heat of ablation; (b) threshold fluence. Open (closed) symbols are used for predominantly protein-(water)-targeting wavelengths. The error bars denote 95% confidence limits. The two overlapping lines in A correspond to the best fits from ANCOVA with a $1/w^2$ covariate.

The Hibst parameters were also subjected to ANCOVA, but with inverted covariates, either $F(w) = 1/w$ or $1/w^2$. We find a very significant dependence of h_{abl} on $1/w^2$ ($P = 9 \times 10^{-8}$). One could make a similar statement with regard to $1/w$, but that best fit yields an unphysical result – specifically $h_{\text{abl}} < 0$ at large spot sizes. In any case, once the variance attributable to spot-size is removed, there is again no remaining dependence on the targeted chromophore ($P_{\text{target}} = 0.94$ for $F(w) = 1/w^2$). This result is shown graphically in Fig. 2(a), where the best-fit curves for each factor level strongly overlap – so strongly that it is difficult to see the two lines separately ($a = 54 \pm 430 \text{ J/g}$, $b = 15 \pm 1.9 \times 10^6 \text{ J } \mu\text{m}^2/\text{g}$ and $c = -34 \pm 450 \text{ J/g}$). From these results, we conclude that the apparent λ -dependence in Fig. 1 is really just a proxy for an underlying w -dependence.

Similar ANCOVA for Φ_{th} is much less definitive. It indicates a slightly significant dependence on $1/w^2$ ($P = 0.02$), and a slightly insignificant dependence on the targeted

chromophore ($P_{target} = 0.07$). In the entire set of etch depth data, this borderline result is the only one with any dependence on the targeted chromophore.

3.2 Collateral damage

As a second test, we measured thermomechanical collateral damage after ablating corneas at 2.77 and 6.45 μm , the two matching wavelengths with the largest difference in differential absorption. Noting the significant w -dependence above, we initially limited these experiments to matching 50- μm spot sizes at the tissue surface. The minimum beam waist was still λ -dependent – 36 versus 50 μm at $\lambda = 2.77$ or 6.45 μm respectively – so the tissue surface was positioned about 400 μm from the 2.77- μm beam waist. The fluence was thus matched at the tissue surface, but differed by a factor of two when averaged over the tissue thickness.

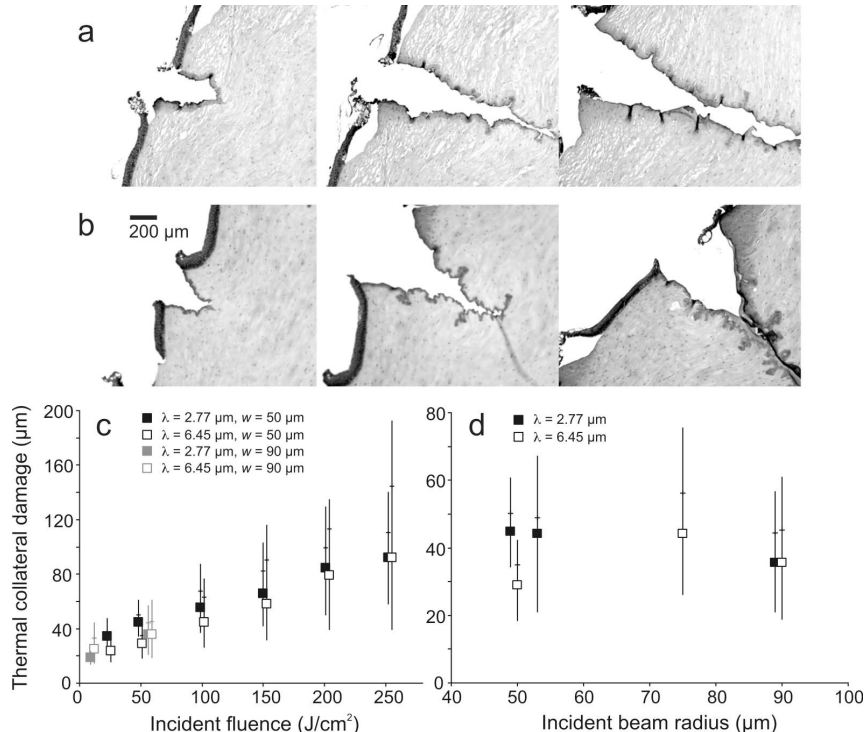


Fig. 3. Wavelength, spot-size and fluence dependence of thermomechanical collateral damage. (a) Selected histological images after FEL ablation of cornea at $\lambda = 2.77 \mu\text{m}$, $w = 50 \mu\text{m}$, and $\Phi = 50, 100$ and 200 J/cm^2 (respectively from left to right). (b) Similar images after ablation at the same spot size and fluence with $\lambda = 6.45 \mu\text{m}$. (c) Collateral damage versus fluence for matched spot sizes. Most points correspond to $w = 50 \mu\text{m}$. Exceptions are in grey and had $w = 90 \mu\text{m}$. (d) Collateral damage at matched fluence ($50\text{-}60 \text{ J/cm}^2$) for different spot sizes. For each set of conditions, the distribution of collateral damage thickness is characterized by its median value (squares), mean value (horizontal dashes) and 1st to 3rd quartile boundaries (vertical lines).

At either λ , higher fluence led to increased collateral damage (Fig. 3). The increased damage is most notable near the tissue surface and at the invaginations/tears in the crater wall. We measured the thickness of collateral damage, Δ , at each position from 10 to 90% of the crater depth and compiled a collateral damage distribution for each λ and Φ . The mean, median and quartile boundaries of the Δ -distributions are plotted in Fig. 3(c). At low fluence, the mean damage widths are significantly different with $1.4 \times$ more damage at $\lambda = 2.77 \mu\text{m}$ ($P = 1 \times 10^{-4}$ at 25 J/cm^2 and $P = 3 \times 10^{-5}$ at 50 J/cm^2 , two-tailed t-test). As Φ increases, the λ -dependence disappears. This fluence-dependence is opposite to the trends predicted by the differential-absorption/partial-confinement model. Note that the damage levels observed here

are certainly larger than those obtained by other lasers in cornea [25], and by the FEL in softer tissues like brain [1]. We are not evaluating the utility of the FEL for cornea surgery, but using cornea as a model tissue for investigating ablation mechanisms.

To see if there was any w -dependence, we also measured the Δ -distributions for larger 90- μm spots. As shown in Fig. 3(c), the damage widths at both spot sizes generally fall along the same trend versus fluence. Interestingly, at the larger spot size, the damage width no longer has a significant λ -dependence at low fluence ($P > 0.1$ at both 12 and 60 J/cm^2). In Fig. 3(d), we compile the Δ -distributions for several experiments with similar fluence (50-60 J/cm^2), but variable spot sizes. The damage has no clear trend with either λ or w .

Importantly, these same histological images confirm a w -dependence for the etch depth. Using just three pulses at $\lambda = 2.77 \mu\text{m}$, $\Phi = 60 \text{ J}/\text{cm}^2$ and $w = 50$ or 90 μm , the larger spot size yielded craters that were $>3 \times$ deeper (680 ± 190 versus $180 \pm 60 \mu\text{m}$). In both cases, the crater width was approximately twice the spot diameter.

3.3 Plume imaging

As a final metric and as a way to investigate the observed spot-size effects, we took images of the ablation plume from 300 ns to 1 ms after the start of the FEL pulse. Image sets were collected for $\lambda = 2.77$ and 6.45 μm with three different lenses ($f = 15, 25$ and 50 cm) and with the pulse energy adjusted to yield a constant fluence of 15 J/cm^2 . In each case, the images revealed a pressure wave followed by a vapor/particulate plume (Fig. 4). The plume was clearly evident by 2-3 μs – well before the end of the FEL macropulse – and dissipated within 100 μs . In a few cases, the 30- and 100- μs images showed a secondary plume from recoil-induced ejection (e.g. 30- μs panel for $\lambda = 6.45 \mu\text{m}$ and $f = 50 \text{ cm}$). The images are very similar to those observed from many examples of photothermal ablation – including ablation of water with an FEL; however, water ablation yielded a longer-lasting plume with much more secondary ejection [22].

We find no discernable λ - or w -dependence for the particulate content of the initial plume, for the speed of the pressure wave ($332 \pm 14 \text{ m/s}$) or for the initial expansion rate of the plume ($156 \pm 13 \text{ m/s}$). The only observable that did vary was the likelihood of secondary ejection. This likelihood increased with spot-size. At $\Phi = 15 \text{ J}/\text{cm}^2$, secondary ejection was always evident for $w > 100 \mu\text{m}$, but was only evident in 1 of 4 experiments with smaller spots.

4. Discussion

We have measured the etch depth and collateral damage for FEL ablation of cornea over a range of λ , w and Φ . These measurements do not confirm the predictions of the differential-absorption/partial-confinement model. The ablation efficiency, or slope of $\delta(\Phi)$, is predicted to have a strong dependence on the targeted chromophore at high fluence ($>15 \text{ J}/\text{cm}^2$), but we find no dependence – once one controls for spot-size effects. The chromophore-dependence of collateral damage is similarly predicted to diverge at high fluence, but we find a convergence. Collateral damage actually increases more quickly with increasing fluence at 6.45 μm . Although previous experiments found a strong λ -dependence for collagen denaturation and fragmentation [19,20], these chemical modifications do not translate here into different ablation metrics. Note that these experiments only contradict predictions based on partial microscale thermal confinement prior to the onset of vaporization [13–15]. Other researchers have previously tested and confirmed predictions based on complete microscale thermal confinement (using shorter pulse lasers and tissues with larger collagen fibers) [26].

Interestingly, the ablation metrics presented here clearly depend on fluence and spot-size. At constant w , both etch depth and collateral damage increase with fluence. At constant Φ , etch depth decreases as spot-size decreases, but collateral damage does not change. The fluence dependence is as expected, but the spot-size dependence is a bit surprising. Although similar spot-size effects have been noted in a few instances [27–29], most ablation studies implicitly assume that making constant fluence comparisons eliminates spot-size effects. In the present data, that assumption is clearly not valid.

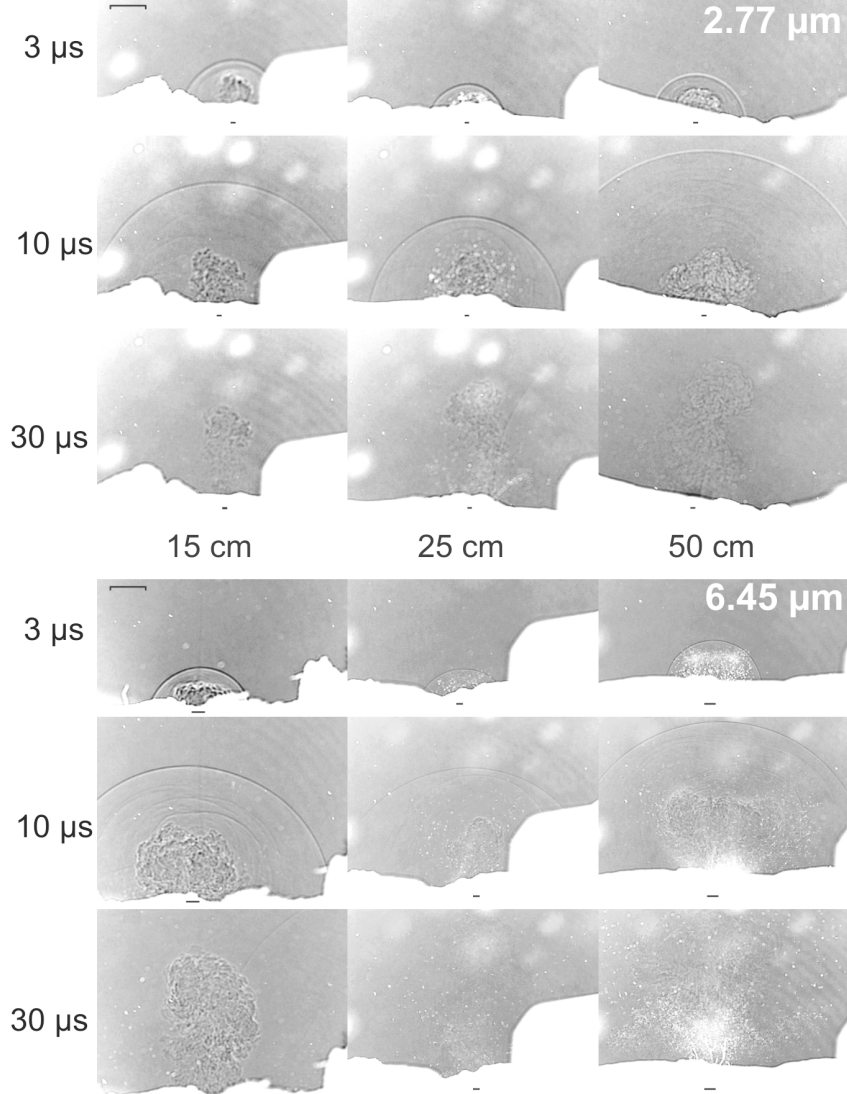


Fig. 4. Bright-field images of the pressure wave and vapor/debris plume during FEL ablation of cornea at $\Phi = 15 \text{ J/cm}^2$ and $\lambda = 2.77 \mu\text{m}$ (top) or $6.45 \mu\text{m}$ (bottom). Each 3×3 set of images has columns for different focusing lenses (nominal $f = 15, 25$ and 50 cm) and rows for different times after the rising edge of the laser pulse ($3, 10$ and $30 \mu\text{s}$). The scale bar at the top left of each image group represents 1 mm . The horizontal bar at the bottom center of each image denotes the measured beam diameter at the tissue surface.

The data presented here on spot-size dependence are not sufficient to pinpoint an exact mechanism. The literature contains many theoretical and empirical examples of spot-size dependencies in ablation, for example:

- A. scattering of more photons out of tightly focused spots [30];
- B. increased plume shielding at larger spots [31,32];
- C. increased loss of energy density in small spots due to heat conduction [33];
- D. influence of tissue curvature on the pressure head needed to stretch the tissue to tensile failure [34]; and
- E. influence of crater aspect ratio on the hydrodynamics of post-pulse ablation [35–37].

We can reasonably eliminate mechanisms A-C: scattering is unlikely to play a large role for mid-IR wavelengths; plume shielding typically decreases ablation efficiency at large spots – opposite to what we observe; and heat diffusion in the radial direction is unlikely to have any impact when tissue removal occurs on times much shorter than the radial thermal diffusion time (<100 μ s compared to 10-200 ms for the spot-sizes used here). Mechanism D is also difficult to justify. A larger pressure head should drive larger initial plume velocities; however, we observe plume velocities with no w -dependence. As for mechanism E, some models of post-pulse or recoil-induced ablation predict a spot-size dependence opposite to that observed [37], but empirical observations show that larger spot sizes lead to longer post-pulse ablation [24,35] – which in turn increases ablation efficiency [36]. Our plume images confirm more post-pulse ablation at larger spot sizes; and our crater images show signs of tearing along the crater walls, as often happens when recoil-induced ejection is somewhat constrained by a mechanically strong tissue [38]. Interestingly, two previous FEL ablation experiments reported wavelength-dependent differences in the post-pulse pressure transients [17,18]. In both cases, the results support the finding here that larger spot sizes lead to more post-pulse ablation. At this point, we consider the primary candidate mechanism to be the hydrodynamics of post-pulse ablation. This effect may be exacerbated by the high aspect ratio craters created here.

Regardless of mechanism, we observe a spot-size and fluence dependence that can conspire to make an apparent wavelength-dependence – particularly when using a single lens and working at a tight beam focus ($w < 100 \mu\text{m}$). If pulse energy is constant, then longer wavelengths have a smaller fluence, which leads to similar etch depths, but less long- λ collateral damage. If fluence is constant, then the spot-size effects lead to similar collateral damage, but higher long- λ ablation efficiency. The latter effect is evident in Fig. 1(a) where wavelength really serves as a proxy for spot size. Note that both combinations lead to better ablation performance at longer wavelengths. These effects could have influenced previous FEL experiments that compared wavelengths at different spot sizes, but there are also FEL experiments that used large, uniform spot sizes by positioning the tissue surface well away from the beam waist [2,21,22,39,40].

Even with these potential complications, our results confirm that FEL pulses in the 6- μm wavelength range do ablate tissue cleanly and efficiently. We do find conditions under which these FEL wavelengths ablate cornea with less collateral damage than other wavelengths. On the other hand, our results also show that $\lambda = 3.32$ or $2.77 \mu\text{m}$ can ablate tissue just as well, simply by adjusting the spot size. This observation is consistent with the known ablation capabilities of Er:YAG and Er:YSSG lasers at $\lambda = 2.94$ and $2.79 \mu\text{m}$ [5–8]. We do not know if the converse is true, i.e. whether the performance of 6- μm lasers will suffer at more tightly focused spots. We also do not know if these trends will hold in more surgically relevant tissues, particularly mechanically weak tissues like brain. Each of these questions will need further investigation as development proceeds on tabletop replacements for the FEL [11,12].

Acknowledgements

The authors thank Prof. Glenn Edwards for reviewing an early version of the manuscript and the staff of the W. M. Keck Vanderbilt Free-electron Laser Center for generously providing beam time and expertise to this project. This work was supported by: grants FA9550-04-1-0045 and FA9620-00-1-0370 from the DoD Medical FEL Program; NSF/HRD grant No. 0420516 (CREST); and by the NSF Center for Biophotonics, managed by U.C. Davis, CA No. PHY0120999.